Graphene-based analog of single-slit electron diffraction

Dipanjan Saha,[1] Dacen Waters,[2,3] Ching-Chen Yeh,[1,4] Swapnil M. Mhatre,[1] Ngoc Thanh Mai Tran,[1,5] Heather M. Hill,[1] Kenji Watanabe,[6] Takashi Taniguchi,[7] David B. Newell,[1] Matthew Yankowitz,[3,8] and Albert F. Rigosi[1,*]

[1]*Physical Measurement Laboratory, National Institute of Standards and Technology (NIST), Gaithersburg, Maryland 20899, USA*
[2]*Intelligence Community Postdoctoral Research Fellowship Program, University of Washington, Seattle, Washington 98195, USA*
[3]*Department of Physics, University of Washington, Seattle, Washington 98195, USA*
[4]*Department of Physics, National Taiwan University, Taipei 10617, Taiwan*
[5]*Joint Quantum Institute, University of Maryland, College Park, Maryland 20742, USA*
[6]*Research Center for Functional Materials, National Institute for Materials Science, 1-1 Namiki, Tsukuba 305-0044, Japan*
[7]*International Center for Materials Nanoarchitectonics, National Institute for Materials Science, 1-1 Namiki, Tsukuba 305-0044, Japan*
[8]*Department of Materials Science and Engineering, University of Washington, Seattle, Washington 98195, USA*

(Received 2 August 2023; revised 5 September 2023; accepted 7 September 2023; published 15 September 2023)

In this paper, we report on the experimental demonstration of single-slit diffraction exhibited by electrons propagating in encapsulated graphene with an effective de Broglie wavelength corresponding to their attributes as massless Dirac fermions. Nanometer-scale device designs were implemented to fabricate a single-slit followed by five detector paths. Predictive calculations were also utilized to readily understand the observations reported. These calculations required the modeling of wave propagation in ideal case scenarios of the reported device designs to more accurately describe the observed single-slit phenomenon. This experiment was performed at room temperature and 190 K, where data from the latter highlighted the exaggerated asymmetry between electrons and holes, recently ascribed to slightly different Fermi velocities near the *K* point. This observation and device concept may be used for building diffraction switches with versatile applicability.

DOI: 10.1103/PhysRevB.108.125420

I. INTRODUCTION

Graphene continues to serve as a unique material for many applications due to its desirable electrical properties [1–4]. More specifically, its high carrier mobility, linear dispersion relation, and lack of a band gap make it possible to create devices essential for electron optics [5–12], including elements like graphene *p-n* junctions that allow for dissipationless edge current flow or reflective surfaces for bulk currents [11–15]. Fully understanding coherent electron propagation in nanoscale devices is crucial for electron optics, and one phenomenon relevant to this understanding is electron coherence, which is known to be observable at micrometer and submicrometer distances [16–20]. At these length scales, electronic transport becomes partially governed by ballistic as opposed to diffusive transport, though it should be noted that, under certain conditions, hydrodynamic regimes must also be considered [21–25].

Since electrons exhibit effectively massless behavior in graphene at energies close enough to the Dirac point, the general question remains whether one can measure some form of wavelike behavior which, in the case of Dirac fermions, would ideally be done with a continuum of detectors [10]. Such devices, especially with improved fabrication techniques, may also form a foundation of a switch mechanism based on diffraction (see Supplemental Material [26]).

In this paper, we report on the observation of single-slit diffraction exhibited by Dirac fermions propagating in graphene fully encapsulated with hexagonal born nitride (*h*-BN) atop a SiO_2 substrate with back-gating compatibility. These massless Dirac fermions appear to have an effective de Broglie wavelength corresponding to their Fermi energy and applied gate voltage (V_g). Device designs on the submicrometer scale were implemented to fabricate a nearly one-dimensional single-slit configuration followed by five detector paths formed with edge contacting [27]. Calculations were performed and required the separate modeling of light-like wave propagation in ideal environments. These separate models incorporated device designs to more accurately describe the observations at room temperature and 190 K. A colder temperature reveals an exaggerated asymmetry of the electrical properties of electrons and holes [2,28–30], with one potential contributing factor being the recently determined observation of differing velocities near the *K* point [28].

II. EXPERIMENTAL AND NUMERICAL METHODS

A. Sample preparation

Devices were fabricated by encapsulating monolayers of graphene between flakes of *h*-BN using standard dry-transfer techniques. A polycarbonate/polydimethyl siloxane stamp was used to assemble the *h*-BN/graphene/*h*-BN stacks and placed onto Si/SiO_2 wafers between prefabricated gold electrodes. Electron beam lithography was used to define the

*albert.rigosi@nist.gov

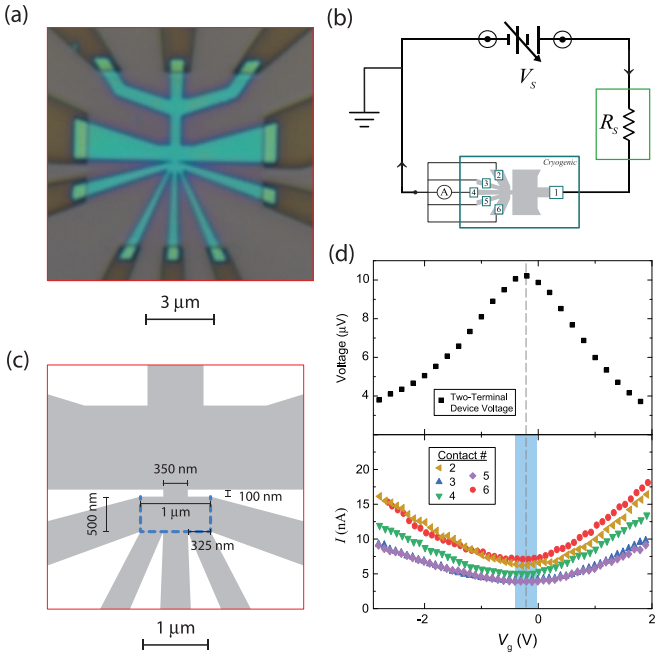

FIG. 1. Graphene single-slit device and basic electrical characterization. (a) An example optical image is shown. The three contacts at the top of the image are to source current into the device and are redundant. (b) A circuit diagram shows how the direct current is permitted to flow through the device. An ammeter is used to collect data for each detection contact. (c) A detailed layout of the effective single-slit device shows the input from the top, a 350 nm slit along the device, and a set of detection paths beyond the dotted blue path. (d) The Dirac point of the device is found by sweeping V_g and measuring the two-terminal voltage (top panel) and standard transfer curves (bottom), yielding about -0.2 V with a standard deviation from the minimum shaded in cyan.

device area in a bubble-free region of the stack via reactive ion etching, and further nanofabrication was performed to establish edge contacts to the graphene layer [27]. The lateral device dimensions are selected to ensure high likelihood of phase coherence and limited detrimental contributions from electron-electron interactions.

A visual representation of an example device is shown in Fig. 1, including illustrations at various magnifications to show the details of the detection contacts. In Fig. 1(c), a detailed layout of the effective single-slit region shows five distinct paths where signals may be collected, with the source of electrons at the top, a 350 nm slit along the device, and a set of detection paths beyond the dotted blue line. The dotted line is crucial in determining various geometric constraints required for simulating expected results.

B. Measurement techniques

To detect the various contributions from each of the detection paths, as drawn in Fig. 1(b), a Keithley 617 electrometer was used (in direct current configuration) to measure the current in each path. The current was supplied by a 1 mV voltage source across a 1 MΩ resistor. The applied current was collected and measured for each detector path. Device testing took place at room temperature to verify electrical contact functionality. Cold temperature measurements took place at 190 K in a cryogen-free cryostat. Device cooling procedures were performed without closed electrical connections to ensure isolation from possible electrostatic discharge.

To determine the Dirac point voltage V_D, two-terminal device voltage data were collected to find the resistive maximum typical of graphene near the Dirac point. Second, a basic transfer curve was obtained while sweeping the gate. Both of these results are shown in the top and bottom panels of Fig. 1(d), where V_D was measured to be about -0.2 V. The bottom panel also shows the standard deviation from the measured -0.2 V minimum as a cyan shaded area.

C. Initial mathematical considerations

Electrons in graphene exhibit massless Dirac behavior, giving them photonlike properties while propagating in a solid medium [2]. It is thus important that predictive calculations correctly incorporate this physical attribute. A major consideration in carrier propagation at these nanometer length scales is their wavelike manifestations, namely, in the form of a de Broglie wavelength, defined as $\lambda_e = \frac{h}{p}$, where the momentum of the electron may be construed in a manner consistent with its properties while in graphene, that is, as a massless Dirac fermion.

To calculate the predicted behavior for this kind of device, one must establish a way in which V_g can be transformed into λ_e. A basic capacitance model is adopted to find the electron density (n_e) as well as the Fermi energy [$E_F = \hbar v_F \sqrt{\pi |n_e|}\mathrm{sign}(n_e)$] [31–33]:

$$V_g - V_D = \frac{e}{C_{ox}} n_e + \frac{\hbar v_F \sqrt{\pi |n_e|}\mathrm{sgn}(n_e)}{e}. \tag{1}$$

In Eq. (1), V_D is the voltage corresponding to the Dirac point, $C_{ox} = \frac{\epsilon_{ox}\epsilon_0}{d_{ox}}$ is the gate capacitance, d_{ox} is the combined thickness of the h-BN and SiO_2 (110 nm) separating the gate and graphene, v_F is the Fermi velocity ($\sim 1.8\times10^6$ m/s initially and will vary as per later discussions), and e is the elementary charge. The used dielectric constant is $\epsilon_{ox} = 3.9$, where ϵ_0 is the vacuum permittivity (the constant is nearly identical for both materials) [31–33]. The final step would be to assume that the majority of charge carriers that are traveling do so at about $E_F = \frac{hc}{\lambda_e}$, where h is the Planck constant, and c is the speed of light.

Calculations are based on conditions of the Fraunhofer regime since the scale of the Fresnel number $F = \frac{a^2}{L\lambda_e}$, with a and L being the slit width (350 nm) and distance to the detector contact (micrometer scales or greater), respectively, is less than the order of unity. With the diffraction condition sufficiently met, one can recall the normalized intensity formula for the single-slit experiment:

$$\frac{K(\theta)}{K_m} = \frac{\sin^2\left(\frac{\pi a}{\lambda_e}\sin\theta\right)}{\left[\frac{\pi a}{\lambda_e}\sin\theta\right]^2} = \mathrm{sinc}^2\left(\frac{\pi a}{\lambda_e}\sin\theta\right). \tag{2}$$

To avoid confusion with electrical current, intensity has been designated as K (with K_m as the maximum intensity for

the wave that has emerged from the slit). The angular bounds relevant for this paper are $\pm\frac{\pi}{2}$, as defined in Fig. 2(a).

III. ROOM-TEMPERATURE DIFFRACTION

To calculate expected device behavior, one must discretize the incoming signal based on the finite number of detector contacts. This discretization is based on the geometrical divisions illustrated in Fig. 2(a), where an example single-slit diffraction pattern is shown in the inset with dashed lines indicating bounds of discretization, which are different due to varying angular ranges. In the ideal case scenario where there exists an infinite number of detectors along a semicircular arc [dotted black line in Fig. 2(a)], one can generate a color map of intensity as a function of V_g and θ, shown in Fig. 2(b). Based on the de Broglie wavelengths of the massless Dirac fermions (on the order of 1000 nm), along with the conditions of small device size to facilitate electronic phase coherence, it is less likely that intensity minima would be observed.

The intensity profile (K/K_m) in Fig. 2(b) may be integrated to yield a normalized spectral density (S/S_m) as a function of detector contact ($C\#$) that will be a proportional representation of the measured electrical current:

$$\frac{S(C\#)}{S_m} = \int_{\theta_2}^{\theta_1} \frac{\sin^2\left(\frac{\pi a}{\lambda_e}\sin\theta\right)}{\left[\frac{\pi a}{\lambda_e}\sin\theta\right]^2} d\theta. \tag{3}$$

This integral must be computed numerically with the appropriate angular bounds (which are: $\pm\frac{\pi}{2}$, $\pm\frac{\pi}{4}$, and about ± 0.3367 rad). The normalizing term S_m considers K_m and π, the total area of the normalized $\mathrm{sinc}^2(x)$ function. This final numerical result is shown in Fig. 3(a) and serves as a basis of comparison for the room-temperature data to be described.

The detected currents of the device at room temperature are shown in Fig. 2(c). If a charge concentrating phenomenon, like diffraction, were not to have occurred, then the fractions of the total measured current present in each detector would have been flat and much closer to the same value (aside from insignificant corrections due to variations in graphene resistance from slightly longer electron paths in the case of some detector contacts). The inherent asymmetries of these data about the Dirac point suggests electron-hole differences that will be addressed later.

One should note that all predictive color maps are not adjusted for V_D but may be easily compared with data after an axis translation. Additionally, values between contacts are interpolated to better visualize rate of change of S/S_m or electrical current, thus giving a clearer picture of whether a predictive model is quantifiably sufficient for describing device behavior. At each value of V_g, the corresponding current through each detector contact is measured with an ammeter dedicated to one detector contact at a time, ultimately yielding Fig. 3(b). By comparing this result to Fig. 3(a), it is clear that the basic model for predictive calculations requires more cautious treatment via mathematical corrections. When incorporating wavelength-dependent transmission (described in the next section), the prediction [Fig. 3(c)] shows a quantifiably noticeable improvement when it comes to describing the observations at room temperature.

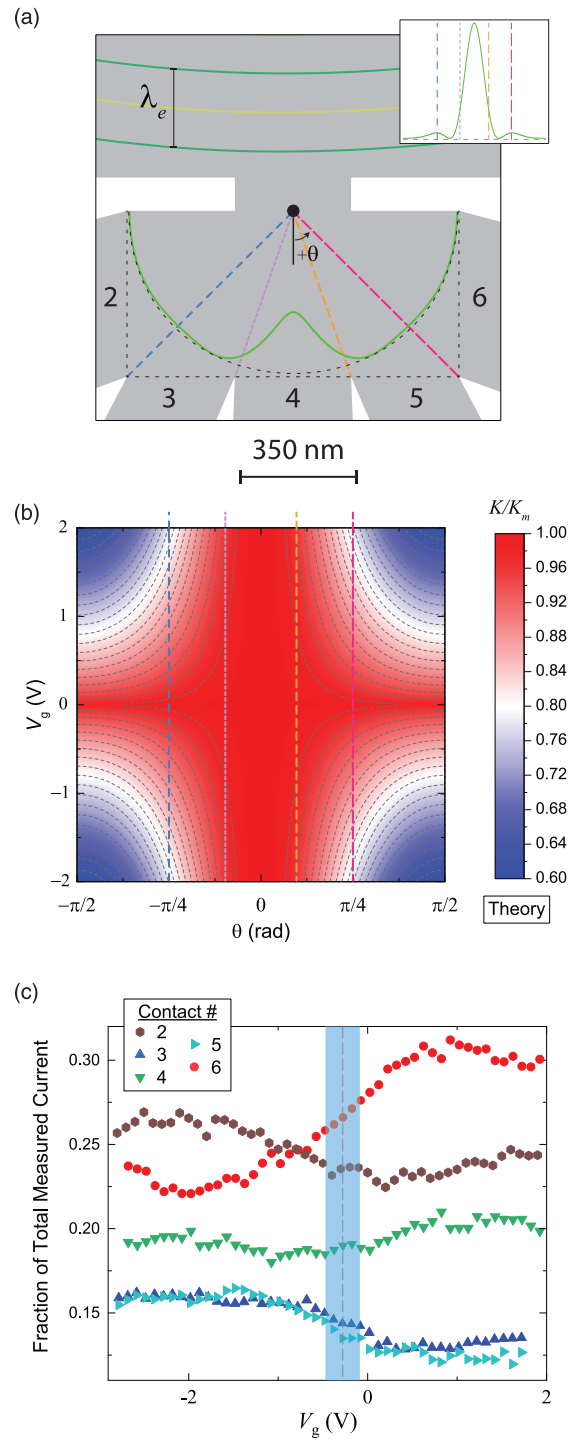

FIG. 2. Measurement configuration and initial prediction. (a) A visual guide is provided to help elucidate the prediction calculations. Contact numbers are assigned to establish clarity in reading most color maps. The blue, purple, orange, and magenta dashed lines (of varying dash length) indicate the angular bounds used per contact and are projected onto the color map in (b). An example single-slit diffraction pattern is shown in the inset as well as projected angularly for visual clarity. (b) The intensity profile (K/K_m) is calculated as a function of angle and gate voltage (V_g), with similar dashed lines showing angular bounds to each detection contact. (c) The fraction of total detected current measured in each contact of the device at room temperature.

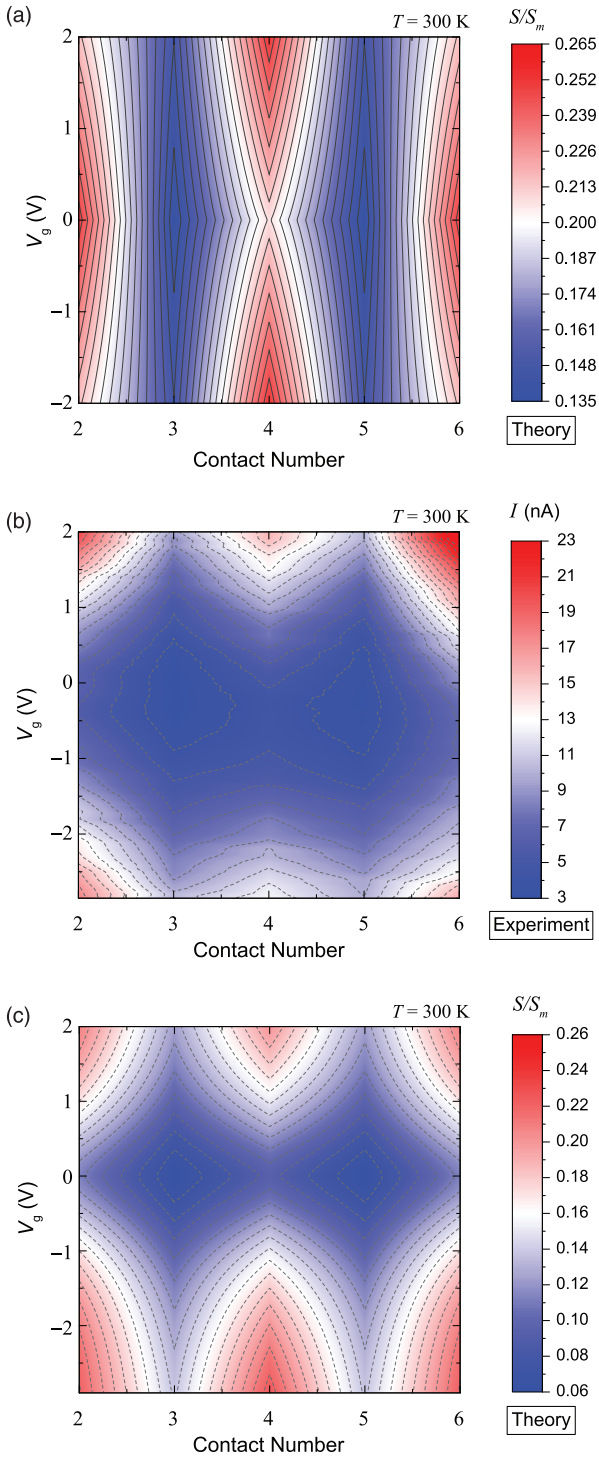

FIG. 3. Room temperature prediction and experimental data. (a) By applying appropriate integration, a predictive color map shows what measurements may yield. Though the simulation is plotted in terms of S/S_m, the experimental data are displayed in nA. (b) The total detected current is measured as a function of V_g and contact number. Comparison of this color plot to (a) reveals that the predictive calculations require a correction. The gray dotted lines represent each subdivision mark on the color scale. (c) Predictive calculation incorporating wavelength-dependent transmission at room temperature. Note that, for all color maps, values between contacts are interpolated to better visualize rate of change of S/S_m or current, thus giving a clearer picture of whether a predictive model is appropriate.

IV. CORRECTIONS AND ELECTRON-HOLE ASYMMETRIES

A. Modeling wavelength-dependent transmission

It is vital to consider whether or not one is dealing with electrons in the hydrodynamic regime [21–25], wherein the Fermi temperature is much smaller than the electron temperature, rendering the system a quantum-critical fluid [34–36]. There is a range of n_e within which this hydrodynamic regime does apply, but a basic calculation shows that the regime would not be significant until n_e falls beneath the order of 10^{11} cm^{-2} [34]. Since most data involve values of n_e greater than this approximate bound, it is not unreasonable to suppose that this regime no longer applies [34–36].

Another consideration is a careful treatment of wavelength-dependent transmission through the single-slit geometry. For this treatment, models of lightlike wave propagation with corresponding length scales were coded and simulated [37–39]. Like Fig. 2(b), each simulation outputs a normalized intensity K/K_0, where K_0 replaces K_m since the latter deals with a maximum value within the set of values pertaining to the transmitted electron signal and the former is meant to represent a full source signal (some of which may reflect off the single-slit geometry). Two example cases of these simulations are shown in Fig. 4(a), and these cases represent a value near the upper bound to the applied gate voltage ($\lambda_e = 1000$ nm) and a value near the Dirac point ($\lambda_e = 5000$ nm).

To approximate the wavelength-dependent transmission numerically over a two-dimensional Cartesian space for each wavelength, the normalized spatiospectral density (J_t/J_0) is calculated by integrating the normalized spectral density of the reflected (J_r) and transmitted (J_t) regions, shown by a green and purple bounded box in Fig. 4(a), respectively. In this approximation, J_0 is the sum total of these two quantities and excludes the spectral densities of the waves that have not yet entered any bounding box. The quantity J_t/J_0 should not be confused with the earlier normalized spectral density pertaining to a signal already transmitted through the single-slit geometry (S/S_m).

These simulations suggest that there is a significant wavelength-dependent transmission, and the relationship may be quantified by the following logistic fit below (where A_1, A_2, x_0, and p are constants):

$$\frac{J_t}{J_0} = \frac{A_1 - A_2}{1 + \left(\frac{\lambda_e}{x_0}\right)^p} + A_2. \tag{4}$$

In Fig. 4(b), the quantity J_t/J_0 is shown as a function of λ_e and fitted with a logistic function, allowing one to introduce a transmission correction to the predictive calculation. This correction, when incorporated into the original prediction from Fig. 3(a) yields the result in Fig. 3(c), which is quantifiably improved when it comes to describing the observations at room temperature. Note that the simulation is centered at 0 V.

B. Electron-hole asymmetry

One interesting observation in the room-temperature data from Fig. 3(b) is the slight hint of asymmetry when com-

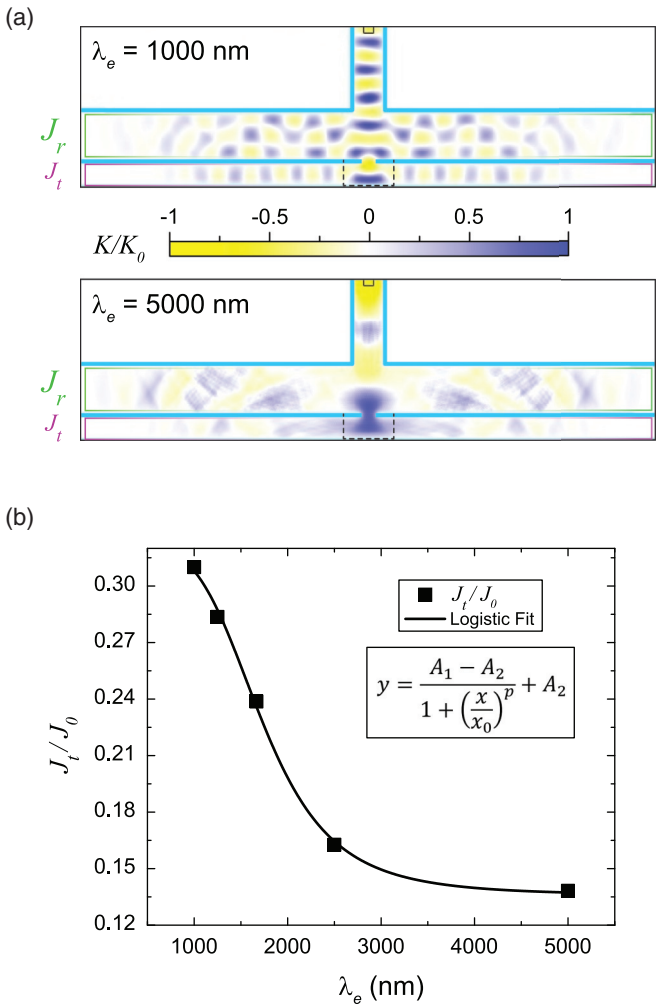

FIG. 4. Approximating wavelength-dependent transmission. (a) Two example simulations are shown that replicate the experimental conditions. The goal of using these simulations is to approximately determine the wavelength-dependence of the electron wave transmission through the single slit. The square of the intensity of the transmitted wave is spatially integrated and compared with J_0. (b) The ratio of these quantities is shown as a function of wavelength and fitted with a logistic function, which is later used to introduce a transmission correction to the predictive calculation.

paring the detected current for holes vs electrons. To reduce any effects from scattering and possibly accentuate any observation of asymmetry, a lower-temperature measurement set was performed at 190 K, shown in Fig. 5 [40]. On the issues of scattering mechanisms, the measured high device mobilities [of at least $10^4\,\mathrm{cm}^2/(\mathrm{Vs})$] were comparable with those in Ref. [40]. In that work, it was shown that such high-mobility devices were not likely to be subject to scattering mechanisms associated with completely screened charge impurities but rather subject to those associated with impurities described by an unscreened, unipolar Coulomb potential [40], giving rise to some level of asymmetry. Furthermore, the scattering mechanism weighted on the unscreened Coulomb potential decreases with temperature, as observed in the same work [40].

The repeated measurements of fractions of total current detected and transfer curves at 190 K are shown in Figs. 5(a) and 5(b), with both showing a more pronounced asymmetry between holes and electrons. The standard deviation from the Dirac point minimum (−0.2 V) is shown as a cyan shaded region. Given this observation of asymmetry, an additional level of correction was required.

In approaching how to modify the existing model with reasonable factors, five effects were examined. The first comes from a possible contribution from $p-n$ junctions that form since the electron density tends to change underneath a metallic contact [11,41–43]. Though these contributions show some measurable influence in the literature, they are also specific to the device being measured and thus subject to variation [41]. The second effect may stem from thermionic emission and interband tunneling, but when approximated and compared with the measured device resistances, it only has an impact on the order of 0.1% of that resistance [44]. The third possibility may be a contribution from inherent asymmetries in the point contact flow (conductance) of electrons and holes, which has been shown at cold temperatures to give holes a slightly higher resistance at the relevant device length scales [45]. Though this runs counter to our observed asymmetry behavior, it also does not contribute a significant enough shift to warrant modeling.

The fourth and fifth effects were modeled in more detail, as they were found to contribute significantly to the observed asymmetry. The fourth effect involves the expected changes to the density of states of graphene when the next-nearest-neighbor hopping parameter (determined to be ∼100meV [30]) becomes nonzero, breaking the symmetry in the density of states near the Dirac point [2]. Since the ratio between the next-nearest- and nearest-neighbor hopping parameters is ∼1:30 [2,30], one can recalculate n_e and adjust accordingly [2]. See the Supplemental Material [26] for an updated model that only considers the change in density of states symmetry.

The fifth effect makes the largest contribution to the asymmetry, namely, that experimental data have shown an asymmetry in the Fermi velocity for electrons and holes [28]. The main reasons for the observed differences in velocity included a variable long-range Coulomb coupling strength as well as a dependency on n_e of the dielectric screening environment, though it should be noted that the latter also depends on the former. The reported logarithmic model was implemented into these models, yielding the final result in Fig. 5(c). When compared with the experimental data in Fig. 5(d), one finds improved agreement. Ergo, it is not unreasonable to posit that any future endeavors seeking to further explore these nanoscale devices should carefully consider the overall effects to the wavelike behaviors of massless Dirac fermions, namely, wavelength-dependent transmission, asymmetries in the density of states, and varying Fermi velocities from long-range Coulomb coupling.

This demonstration of electron diffraction through a commensurate slit opens the door for further study of alternative fabrication techniques to more precisely control slit edge quality and subsequently check effects on the observed diffraction pattern. Applications involving multiple slits that are gated to control transmission through the slit may be relevant in both electronics and photonics, especially with

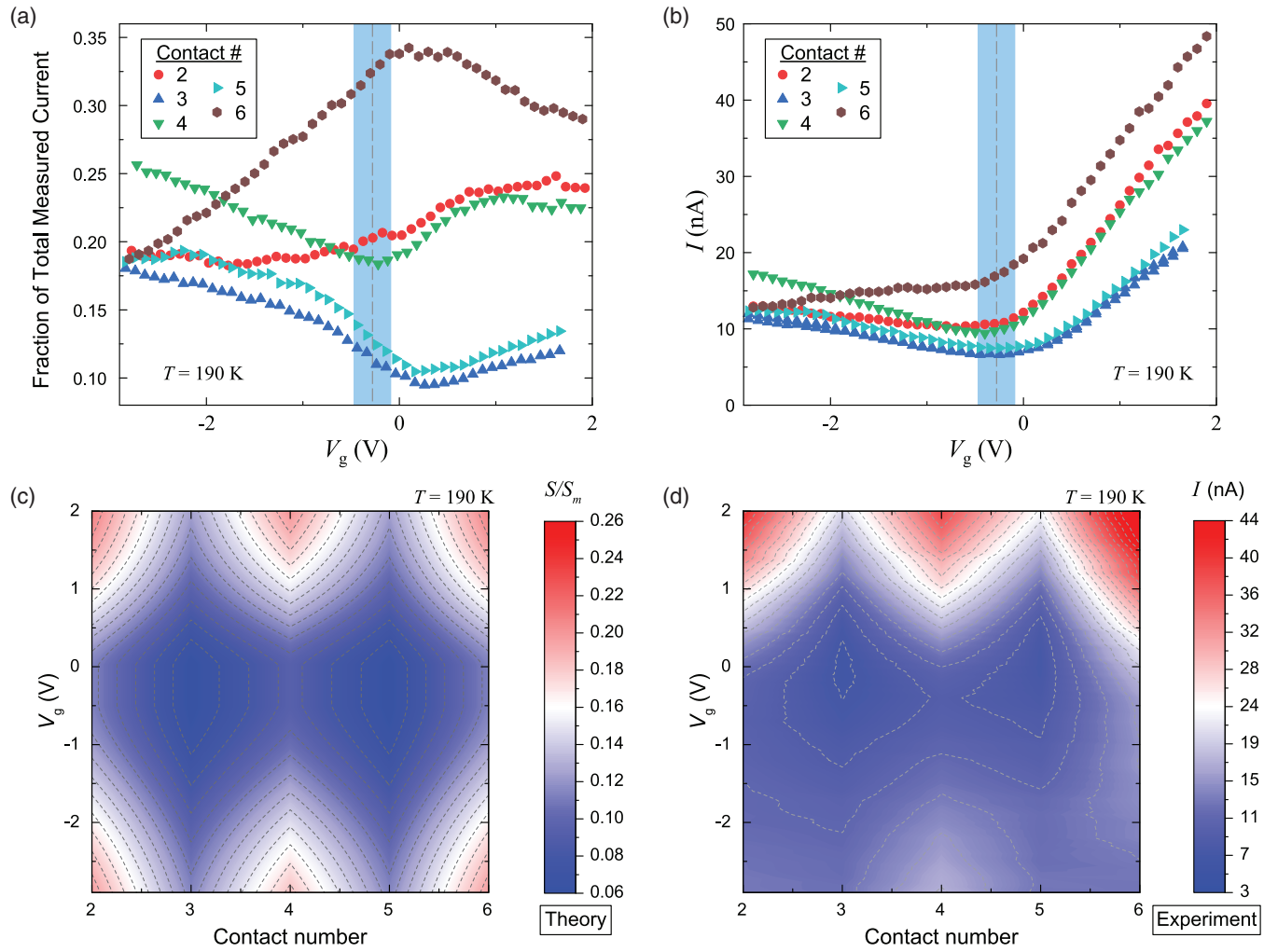

FIG. 5. Final model and the asymmetry between electrons and holes (at 190 K). (a) The fraction of total detected current measured in each contact of the device. (b) Transfer curves were obtained, with the standard deviation from the −0.2 V Dirac point minimum shown as a cyan shaded region. (c) When considering the effects of electron and hole asymmetry, predictive calculations were performed to compare with corresponding experimental data shown in (d). The gray dotted lines in all color graphs represent each subdivision mark on the corresponding scale.

devices based on bilayer graphene, where gating can open a band gap.

V. CONCLUSIONS

In this paper, observations of single-slit diffraction are reported as being exhibited by massless Dirac fermions propagating in fully encapsulated graphene. The charge carriers are suggested, based on corresponding models, to have an effective de Broglie wavelength related to their Fermi energies and applied gate voltages (V_g). Nanoscale device designs and sophisticated fabrication techniques allowed for the construction of a nearly one-dimensional single-slit configuration, followed by five detector contacts. Observed nanoscale device behavior prompted the consideration of many possible contributing effects, with the most prominent reasonably attributed to wavelength-dependent transmission, charge carrier asymmetries in the density of states, and varying Fermi velocities from long-range Coulomb coupling.

ACKNOWLEDGMENTS

For fruitful discussions and interactions, the authors thank A. L. Levy, E.-M. Shih, T. T. Mai, A. R. Hight Walker, and Heidelberg Instruments. The authors also thank M. F. Munoz, F. Fei, G. J. Fitzpatrick, and E. C. Benck for their assistance with the NIST internal review process. D.W. was supported by an appointment to the Intelligence Community Postdoctoral Research Fellowship Program at the University of Washington (UW) administered by the Oak Ridge Institute for Science and Education through an interagency agreement between the U.S. Department of Energy and the Office of the Director of National Intelligence. Device fabrication at UW was supported by the National Science Foundation CAREER Award No. DMR-2041972. Work presented herein was performed, for a subset of the authors, as part of their official duties for the U.S. Government. Funding is hence appropriated by the U.S. Congress directly.

The authors declare no competing interest.

[1] A. K. Geim and K. S. Novoselov, Nat. Mater. **6**, 183 (2007).
[2] A. H. Castro Neto, F. Guinea, N. M. R. Peres, K. S. Novoselov, and A. K. Geim, Rev. Mod. Phys. **81**, 109 (2009).
[3] K. S. Novoselov, V. I. Fal'ko, L. Colombo, P. R. Gellert, M. G. Schwab, and K. A. Kim, Nature (London) **490**, 192 (2012).
[4] S. Das Sarma, S. Adam, E. H. Hwang, and E. Rossi, Rev. Mod. Phys. **83**, 407 (2011).
[5] S. Chen, Z. Han, M. M. Elahi, K. M. Masum Habib, L. Wang, B. Wen, Y. Gao, T. Taniguchi, K. Watanabe, J. Hone *et al.*, Science **353**, 1522 (2016).
[6] R. N. Sajjad and A. W. Ghosh, Appl. Phys. Lett. **99**, 123101 (2011).
[7] M. M. Elahi, K. M. Masum Habib, K. Wang, G.-H. Lee, P. Kim, and A. W. Ghosh, Appl. Phys. Lett. **114**, 013507 (2019).
[8] V. V. Cheianov, V. Fal'ko, and B. L. Altshuler, Science **315**, 1252 (2007).
[9] Y. Zhao, J. Wyrick, F. D. Natterer, J. F. Rodriguez-Nieva, C. Lewandowski, K. Watanabe, T. Taniguchi, L. S. Levitov, N. B. Zhitenev, and J. A. Stroscio, Science **348**, 672 (2015).
[10] P. Bøggild, J. M. Caridad, C. Stampfer, G. Calogero, N. R. Papior, and M. Brandbyge, Nat. Commun. **8**, 15783 (2017).
[11] B. Huard, J. A. Sulpizio, N. Stander, K. Todd, B. Yang, and D. Goldhaber-Gordon, Phys. Rev. Lett. **98**, 236803 (2007).
[12] H. Schmidt, J. C. Rode, C. Belke, D. Smirnov, and R. J. Haug, Phys. Rev. B **88**, 075418 (2013).
[13] D. K. Patel, M. Marzano, C.-I. Liu, H. M. Hill, M. Kruskopf, H. Jin, J. Hu, D. B. Newell, C.-T. Liang, R. E. Elmquist *et al.*, AIP. Adv **10**, 025112 (2020).
[14] A. F. Rigosi, M. Marzano, A. Levy, H. M. Hill, D. K. Patel, M. Kruskopf, H. Jin, R. E. Elmquist, and D. B. Newell, Physica B **582**, 411971 (2020).
[15] J. Hu, A. F. Rigosi, J. U. Lee, H.-Y. Lee, Y. Yang, C.-I. Liu, R. E. Elmquist, and D. B. Newell, Phys. Rev. B **98**, 045412 (2018).
[16] F. Miao, S. Wijeratne, Y. Zhang, U. C. Coskun, W. Bao, and C. N. Lau, Science **317**, 1530 (2007).
[17] M. T. Allen, O. Shtanko, I. C. Fulga, J. I.-J. Wang, D. Nurgaliev, K. Watanabe, T. Taniguchi, A. R. Akhmerov, P. Jarillo-Herrero, L. S. Levitov *et al.*, Nano Lett. **17**, 7380 (2017).
[18] W. Liang, M. Bockrath, D. Bozovic, J. H. Hafner, M. Tinkham, and H. Park, Nature (London) **411**, 665 (2001).
[19] Y. Wu, V. Perebeinos, Y. Lin, T. Low, F. Xia, and P. Avouris, Nano Lett. **12**, 1417 (2014).
[20] S. Engels, B. Terrés, A. Epping, T. Khodkov, K. Watanabe, T. Taniguchi, B. Beschoten, and C. Stampfer, Phys. Rev. Lett. **113**, 126801 (2014).
[21] D. A. Bandurin, I. Torre, R. Krishna Kumar, M. Ben Shalom, A. Tomadin, A. Principi, G. H. Auton, E. Khestanova, K. S. Novoselov, I. V. Grigorieva *et al.*, Science **351**, 1055 (2016).
[22] P. O. Sukhachov and E. V. Gorbar, Phys. Rev. B **104**, 195111 (2021).
[23] A. Lucas and K. C. Fong, J. Phys.: Condens. Matter **30**, 053001 (2018).
[24] A. I. Berdyugin, S. G. Xu, F. M. D. Pellegrino, R. Krishna Kumar, A. Principi, I. Torre, M. Ben Shalom, T. Taniguchi, K. Watanabe, I. V. Grigorieva *et al.*, Science **364**, 162 (2019).
[25] A. Block, A. Principi, N. C. H. Hesp, A. W. Cummings, M. Liebel, K. Watanabe, T. Taniguchi, S. Roche, F. H. L. Koppens, N. F. van Hulst *et al.*, Nat. Nanotechnol. **16**, 1195 (2021).
[26] See Supplemental Material at http://link.aps.org/supplemental/10.1103/PhysRevB.108.125420 for alternate simulation information and potential applications.
[27] L. Wang, I. Meric, P. Y. Huang, Q. Gao, Y. Gao, H. Tran, T. Taniguchi, K. Watanabe, L. M. Campos, D. A. Muller *et al.*, Science **342**, 614 (2013).
[28] N. Dale, R. Mori, M. I. B. Utama, J. D. Denlinger, C. Stansbury, C. G. Fatuzzo, S. Zhao, K. Lee, T. Taniguchi, K. Watanabe *et al.*, npj Quantum Mater. **7**, 9 (2022).
[29] K. S. Novoselov, A. K. Geim, S. V. Morozov, D. Jiang, M. I. Katsnelson, I. V. Grigorieva, S. V. Dubonos, and A. A. Firsov, Nature (London) **438**, 197 (2005).
[30] R. S. Deacon, K.-C. Chuang, R. J. Nicholas, K. S. Novoselov, and A. K. Geim, Phys. Rev. B **76**, 081406(R) (2007).
[31] S. Kim, J. Nah, I. Jo, D. Shahrjerdi, L. Colombo, Z. Yao, E. Tutuc, and S. K. Banerjee, Appl. Phys. Lett. **94**, 062107 (2009).
[32] K. Takase, H. Hibino, and K. Muraki, Phys. Rev. B **92**, 125407 (2015).
[33] K. Takase, S. Tanabe, S. Sasaki, H. Hibino, and K. Muraki, Phys. Rev. B **86**, 165435 (2012).
[34] D. E. Sheehy and J. Schmalian, Phys. Rev. Lett. **99**, 226803 (2007).
[35] H. Y. Xie and M. S. Foster, Phys. Rev. B. **93**, 195103 (2016).
[36] A. Lucas, J. Crossno, K. C. Fong, P. Kim, and S. Sachdev, Phys. Rev. B. **93**, 075426 (2016).
[37] M. Ghalandari and M. Solaimani, Sci. Rep. **10**, 19458 (2020).
[38] D. K. Kalluri, *Electromagnetic Waves, Materials, and Computation with MATLAB*® (CRC Press, Boca Raton, 2011).
[39] P. Falstad, 2019. Falstad Simulation Applets. http://www.falstad.com/mathphysics.html.
[40] S. Sarkar, K. R. Amin, R. Modak, A. Singh, S. Mukerjee, and A. Bid, Sci. Rep. **5**, 16772 (2015).
[41] S. Lee, A. Nathan, J. Alexander-Webber, P. Braeuninger-Weimer, A. A. Sagade, H. Lu, D. Hasko, J. Robertson, and S. Hofmann, ACS Appl. Mater. Interfaces **10**, 10618 (2018).
[42] J. R. Williams, L. DiCarlo, and C. M. Marcus, Science **317**, 638 (2007).
[43] T. Low, S. Hong, J. Appenzeller, S. Datta, and M. S. Lundstrom, IEEE Trans. Electron Dev. **56**, 1292 (2009).
[44] A. Satou, G. Tamamushi, K. Sugawara, J. Mitsushio, V. Ryzhii, and T. Otsuji, IEEE Trans. Electron Dev. **63**, 3300 (2016).
[45] R. Krishna Kumar, D. A. Bandurin, F. M. D. Pellegrino, Y. Cao, A. Principi, H. Guo, G. H. Auton, M. Ben Shalom, L. A. Ponomarenko, G. Falkovich *et al.*, Nat. Phys. **13**, 1182 (2017).